

See discussions, stats, and author profiles for this publication at: <https://www.researchgate.net/publication/280104978>

How Common are Hot Magnetic Flux Ropes in the Low Solar Corona? A Statistical Study of EUV Observations

Article in *The Astrophysical Journal* · July 2015

DOI: 10.1088/0004-637X/808/2/117 · Source: arXiv

CITATIONS

17

READS

97

4 authors, including:



Spiros Patsourakos

121 PUBLICATIONS 1,654 CITATIONS

[SEE PROFILE](#)



Angelos Vourlidas

Johns Hopkins University

423 PUBLICATIONS 8,292 CITATIONS

[SEE PROFILE](#)



Christos Tagikas

Aristotle University of Thessaloniki

1 PUBLICATION 17 CITATIONS

[SEE PROFILE](#)

Some of the authors of this publication are also working on these related projects:



Solar Terrestrial Relations Observatory [View project](#)



SECCHI/STEREO [View project](#)

Draft version of July 15, 2015

How Common are Hot Magnetic Flux Ropes in the Low Solar Corona? A Statistical Study of EUV Observations

A. Nindos and S. Patsourakos

Section of Astrogeophysics, Physics Department, University of Ioannina, Ioannina, Greece

anindos@uoi.gr

A. Vourlidas

The Johns Hopkins University Applied Physics Laboratory, Laurel MD, USA

and

C. Tagikas

Section of Astrogeophysics, Physics Department, University of Ioannina, Ioannina, Greece

ABSTRACT

We use data at 131, 171, and 304 Å from the Atmospheric Imaging Assembly (AIA) aboard the Solar Dynamics Observatory (SDO) to search for hot flux ropes in 141 M-class and X-class solar flares that occurred at solar longitudes equal to or larger than 50°. Half of the flares were associated with coronal mass ejections (CMEs). The goal of our survey is to assess the frequency of hot flux ropes in large flares irrespective of their formation time relative to the onset of eruptions. The flux ropes were identified in 131 Å images using morphological criteria and their high temperatures were confirmed by their absence in the cooler 171 and 304 Å passbands. We found hot flux ropes in 45 of our events (32% of the flares); 11 of them were associated with confined flares while the remaining 34 were associated with eruptive flares. Therefore almost half (49%) of the eruptive events involved a hot flux rope configuration. The use of supplementary Hinode X-Ray Telescope (XRT) data indicates that these percentages should be considered as lower limits of the actual rates of occurrence of hot flux ropes in large flares.

Subject headings: Sun: flares – Sun: coronal mass ejections

1. Introduction

Coronal mass ejections (CMEs) are large-scale expulsions of coronal plasma and magnetic field entrained therein into the heliosphere. Several models of CME initiation have been developed (e.g.

Chen 2011, and references therein). All models agree that CMEs may result from a catastrophic loss of mechanical equilibrium of plasma confined by the coronal magnetic field. However, there is no consensus about the pre-eruptive magnetic configuration; the CME models can be divided into two groups depending on the state of the coronal magnetic field prior to the eruption. The models of the first group assume that a magnetic flux rope (i.e. a coherent magnetic structure of magnetic field lines that collectively wind about a central, axial field line) exists prior to the eruption (e.g. Forbes and Isenberg 1991; Forbes and Priest 1995; Gibson and Low 1998; Titov and Démoulin 1999; Roussev et al. 2003; Amari et al. 2004; 2005; Fan and Gibson 2004; 2007; Archontis and Török 2008; Fan 2010; Archontis and Hood 2012). The models of the second group rely on the existence of sheared magnetic arcades (i.e. an arrangement of loops with planes deviating significantly from the local normal to the polarity inversion line) that become unstable and erupt once some critical state is reached in the corona (e.g. Linker and Mikić 1995; Amari et al. 1999; 2000; Antiochos et al. 1999; Manchester 2003; Roussev et al. 2004; MacNeice et al. 2004; Jacobs et al. 2006; van der Holst 2007; Lynch et al. 2008; Archontis and Hood 2008; Karpen et al. 2012).

While the question on which pre-eruptive magnetic configuration leads to CMEs is open, all models and simulations agree that the erupting structure is a flux rope. There is no physical mechanism that can produce a large-scale eruption from the corona without ejecting a flux rope, except under very specific magnetic configurations (Jacobs et al. 2009). In the first group of models the flux rope is an essential ingredient of the pre-eruptive configuration while in the second group of models the flux rope is formed once the CME is underway, i.e., on-the-fly.

Indirect evidence for the existence of pre-eruptive flux ropes in active regions (ARs) located close to disk center comes from non-linear force-free field (NLFFF) extrapolations that use data from photospheric vector magnetograms as boundary condition (e.g. Yan et al. 2001; Bleybel et al. 2002; Canou et al. 2009; Guo et al. 2010; 2012; Sun et al. 2012; Nindos et al. 2012; Jiang & Feng 2013; Cheng et al. 2014b). The temporal resolution of NLFFF extrapolations is determined by the cadence of the available vector magnetograms which, is currently 12 minutes, at best. Therefore, the extrapolation products are unable to capture the rapidly-changing magnetic fields that erupt. Furthermore, there is a non-vanishing Lorentz force that makes the magnetic field non-force-free, once the eruption gets underway.

Another piece of indirect evidence for pre-existing flux ropes are soft X-ray (SXR) and EUV observations of S- or reverse S-shaped (sigmoidal) regions. Sigmoidal ARs have a high likelihood of producing an eruption (e.g. Canfield et al. 1999). If a sigmoidal source of SXR or EUV emission, which follows the magnetic field lines, crosses the polarity inversion line in the inverse direction of what a potential arcade would do then it is considered as disk signature of a flux rope viewed from above. This, however, is conclusive only if the sigmoidal source survives an eruption (e.g. Gibson & Fan 2006; Green & Kliem 2009; Green et al. 2011), because only then S-shaped field lines in a sheared arcade (Antiochos et al. 1994) can be excluded.

Yohkoh (Ogawara et al. 1991) Soft X-ray Telescope (SXT; Tsuneta et al. 1991) data (Ohyama

& Shibata 1998; 2008; Nitta & Akiyama 1999; Kim et al. 2004; 2005a,b) and *Hinode* (Kosugi et al. 2007) X-Ray Telescope (XRT; Golub et al. 2007) data (Savage et al. 2010; Landi et al. 2013; Lee et al. 2015) have revealed the existence of hot ejecta during CMEs. The ejecta formed coherent hot structures but in most of these publications were not identified as magnetic flux ropes.

The availability of high sensitivity data recorded with unprecedented spatial and temporal resolution in hot, flare-like EUV wavelengths by the Atmospheric Imaging Assembly (AIA; Lemen et al 2012) aboard the Solar Dynamics Observatory (SDO; Pesnell et al. 2012) confirmed the existence of coherent structures identified as hot flux ropes (Reeves & Golub 2011; Cheng et al. 2011, 2012, 2013, 2014a,b,c; Zhang et al. 2012; Li & Zhang 2013; Patsourakos et al. 2013; Joshi et al. 2014; Song et al. 2014). The heating of the flux rope may be a consequence of magnetic reconnection. The standard solar eruption model predicts that the reconnected magnetic flux under the CME is channeled into both the flare loops and the erupting flux rope.

Several case studies of hot flux ropes associated with impulsive CMEs have been published. The main focus of these publications was the question of whether the flux rope forms before or during the eruption. Most studies were in favor of pre-existing flux ropes (Zhang et al. 2012; Patsourakos et al. 2013; Li & Zhang 2013; Cheng et al. 2013; 2014a; 2014b; 2014c) although cases of hot flux ropes formed on-the-fly during the eruption (Cheng et al. 2011; Song et al. 2014) have been reported as well as cases of hot flux ropes involved in confined eruptions (Patsourakos et al 2013; Cheng et al. 2014b; Joshi et al. 2014). All these events originated in active regions close to the solar limb.

These works were exclusively single-event studies, leaving an unclear picture on the role/importance of hot flux ropes in CMEs. To remedy this situation, we undertake the present study to search for hot flux rope events using an extensive dataset of large flares that occurred away from disk center. To keep this paper focused, we do not address the question on whether the flux ropes formed before or during the eruptions. Instead, we address the more fundamental question of how common hot flux ropes are in the low corona. Our aim is to place past and future case studies in a broader context. Our paper is organized as follows. The observations and data analysis are presented in Section 2. Our classification scheme is introduced in Section 3. In Section 4 we discuss the events with hot flux ropes and in Section 5 the events without hot flux rope morphology. In Section 6 we compare the AIA data with data obtained from the *Hinode* XRT. We conclude in Section 7.

2. Observations and Data Analysis

We have compiled a catalog of M-class and X-class flares that occurred from early November 2010 until the end of March 2014 at longitudes equal to or larger than 50° from central meridian. We selected events away from disk center because the identification of flux ropes becomes easier due to projection effects. We set an M-class threshold because the higher energy release is more likely to produce hot flux ropes. We do not preclude the existence of flux ropes in other flare

types. Our catalog consists of 141 events. We analyzed each event using EUV images of the low corona from the SDO/AIA. The field of view, pixel size, and cadence of the AIA images are $1.3R_{\odot}$, $0.6''$, and 12 s, respectively. To reduce data volume, we used AIA images with a cadence of 1 minute. Inspection of full cadence movies of selected events showed that the one minute cadence was sufficient to resolve the various dynamics.

We used AIA images in narrowband channels centered at 131, 171, and 304 Å. In the remainder of the paper we will refer to any given channel by simply supplying the wavelength of peak response: for example, 131 Å channel will be referred to as 131. The 131 emission arises from two dominant ions formed at different temperatures: Fe VIII at 4×10^5 K and Fe XXI at 10^7 K (Lemen et al. 2012). The signal in 131 is dominated by multi-million plasma only during flares. The dominant ions in the 171 and 304 channels are Fe IX and He II, respectively. Their peak formation temperatures are 6×10^5 K and 5×10^4 K, respectively (Lemen et al. 2012).

In addition to the AIA data we used white-light coronagraph data from the Large Angle Spectroscopic Coronagraph (LASCO; Brueckner et al 1995) C2 coronagraph on board the Solar and Heliospheric Observatory (SOHO; Domingo et al 1995) mission. The LASCO C2 field of view covers the range of $2.2\text{--}6R_{\odot}$ with a pixel size of $12''$, and nominal cadence of 12 minutes during the period of our observations. For the overall temporal evolution of the flares, we used GOES X-ray total flux measurements.

Our first analysis step was to search for signatures of hot flux ropes in 131 movies. The observed morphology of flux ropes depends on its inherent twist and viewing angle but their identification is often challenging because: (1) the hot flux rope emission at 131 Å may be weak, (2) more often than not, flux ropes are weakly twisted, and (3) other structures (e.g. loops), and saturation from the flare may contaminate the line of sight (LOS). Based on our experience, we settled in the following set of criteria for flux rope identification in the 131 images:

1. Flux ropes seen edge-on. They correspond to round blobs or ring-like structures. They appear to overlay structures with a variety of morphologies: Λ -shaped loop-like structures, cusp-like structures or thin elongated emissions presumably associated with current sheets. Examples of flux ropes seen edge-on appear in Figure 1.
2. Flux ropes seen face-on. The clearest cases show tangled threads of emission that appear to wind around an axis. Structures that show a twisted/writhed shape could also be interpreted as flux ropes seen face-on. Examples of flux ropes seen face-on appear in Figure 2.
3. Flux ropes viewed from intermediate angles. They show intermediate morphologies between the morphologies of flux ropes seen edge-on and face-on. Examples are presented in Figure 3.
4. The candidate flux rope should appear in at least two successive 131 Å images.

Because we are searching for hot flux ropes, the candidate structures in the 131 Å data must be hot. An obvious approach would be the calculation of the differential emission measure of the

structures and the subsequent computation of emission measure maps in different temperature intervals. We decided against such approach at this time due to the large size of our database and the added complexity of the DEM calculation procedures. Instead, we adopt a simple, but straightforward approach, to check for the simultaneous appearance of the candidate flux ropes in 171 and 304 movies. If the candidates do not appear in these colder channels then the 131 emission must arise from Fe XXI and hence from 10 MK plasma. We note that this was the case for all candidate hot flux ropes that we identified in 131 data.

We tried especially hard to avoid over-interpretation of the data. Several features have the potential to be misinterpreted as flux ropes. These include cusps, ascending post-CME loops (especially those seen edge-on) and small-scale emission depletions that are not surrounded by clear twisted/writhed structures or ring-like structures, but result from the projection of loops of different shapes and orientations on the plane of the sky.

Finally we used movies of LASCO C2 data to determine whether the events in our database were associated with CMEs. The association was checked for all events of our database, irrespective of being hot flux ropes or not. The CMEs were also classified as flux rope CMEs (FR-CMEs) or not using the criteria defined by Vourlidas et al. (2013).

3. Classification of Events

Our database consists of 141 events shown in Table 1. The first six columns give (from left to right) the event number, the date of the event, the flare start and peak times, the flare location in heliographic coordinates, the NOAA number of the host AR, and the GOES classification of the flare. The seventh column contains the information on the associated CME, if there was one. The eighth column provides our classification of the events into five subcategories.

Overall, 45 flares were associated with hot flux ropes and 96 flares were not. This simple division, however, does not provide much insight into the problem. We refined our classification to reflect the wealth of observed morphologies and eruption paths present in the data. According to this refined scheme, the events were classified in the following groups (Table 1, column 8):

1. Confined flare events with hot flux ropes (CFR in Table 1). No evidence of eruption but detection of a hot flux rope in the AIA images.
2. Eruptions with hot flux ropes (EFR in Table 1). Evidence for the eruptive nature of the events was provided by post-flare/post-CME loops, cusps, or overall opening of the AR’s configuration.
3. Prominence eruption events without hot flux ropes (PE in Table 1).
4. Eruptions without hot flux ropes or prominences (PFL in Table 1).

5. Confined flare events without hot flux ropes (CFL in Table 1). There was no evidence of an eruption or a hot flux rope.

4. Events With Hot Flux Ropes

4.1. Morphology of Hot Flux Ropes

We identified 45 events with hot flux rope morphology; in 34 cases there was an eruption (EFR events of Table 1) and in 11 cases the hot flux rope did not erupt (CFR events of Table 1). Single snapshots of various hot flux ropes in 131 Å are presented in Figures 1-3. In Figure 4 we present the evolution of a confined hot flux rope event while in Figures 5-7 we present the evolution of three eruptive hot flux rope events.

The hot flux ropes can be divided into three categories according to their LOS orientation (see Section 2): (1) hot flux ropes seen edge-on (Figures 1, 4, and 7), (2) hot flux ropes seen face-on (Figures 2 and 6), and (3) hot flux ropes viewed from intermediate angles (Figures 3 and 5).

Our database contains 20 cases of hot flux ropes seen edge-on, 9 cases of hot flux ropes seen face-on and 16 intermediate cases. Most of the previous analyses of hot flux rope events involve flux ropes seen edge-on. Reports on hot flux ropes seen face-on is rather limited (e.g. Li & Zhang 2013, Cheng et al. 2014c, Joshi et al. 2014). The larger proportion of flux ropes seen edge-on can be explained as follows. The LOS integration along a structure seen edge-on is longer than for a face-on case. Flux ropes are expected to run approximately along the neutral line of their host ARs which generally lies along the East-West direction. Therefore, as the AR approaches the limb, the neutral line becomes more and more aligned with a direction parallel to LOS, and consequently its associated flux rope should be seen edge-on.

4.2. Confined Events with Hot Flux Ropes

The confined nature of the CFR events was judged from the EUV data and confirmed from LASCO observations. LASCO data were available for all 11 CFR events and none of them showed evidence for CMEs.

Snapshots of confined events with hot flux ropes are presented in Figure 1 (panels a-d). All of them appear as round blobs of hot plasma which implies that they are seen edge-on. In the event of panel (a), there is thin elongated emission resembling a current sheet just underneath the flux rope. The situation in the event of panels (b), (c), and (d) is less clear in terms of the appearance of current-sheet-like or cusp-like structures, but nevertheless stretched loops that connect the flux rope with the lower atmosphere can be seen.

The evolution of a characteristic CFR event (event 86) is presented in Figure 4 (see also

movie1.mp4). The event took place on 2013 January 5 in AR11652 and was associated with an M1.7-class flare. Figure 4(a) was taken just before the flare onset. The image shows loops of different scales; from low-lying loops to large-scale loops that correspond to the background magnetic field. At about 09:29 in 131 Å a semi-circular bright loop-like feature appears very close to the limb. At 09:30 an initially round blob evolves clear striations by 9:31 (Figure 4b,c). This morphology corresponds to a flux rope seen edge-on. The flux rope appears to sit at the tip of a current-sheet-like structure (Figure 4b,c). During the next two minutes the flux rope moves outward increasing in size. According to the standard flare model, magnetic reconnection induced in the current sheet converts the stretched surrounding field into new poloidal flux of the flux rope. In addition to its ascending motion, it is possible that the flux rope exhibits rotation as well. The rotation changes the orientation of the flux rope with respect to the line of sight and this may explain why its morphology has changed in Figure 4d. We see an elliptical structure with S-shaped threads inside it instead of a round blob. After 09:33 the flux rope stops rising. The associated movie gives the impression that the overlying field acts as an obstacle that inhibits the ascending motion of the flux rope.

The flux rope is visible only in the 131 passband (see the movie, Figure 4f, 4h and the 131/171 and 131/304 composites in panels g and i). Therefore the flux rope temperature is about 10 MK, i.e. it is a *hot* flux rope. Furthermore, the 131/171 composite image shows that the hot flux rope is enclosed in an area of weak 171 Å emission. Several authors have reported (e.g. Cheng et al. 2011, 2013; Zhang et al. 2012) that hot flux ropes are sometimes enclosed in a dark cavity or bubble, observed in cooler emissions, e.g., in the 171 channel. The hot flux rope may not fully occupy the cavity, at least during the initial stages of the EUV cavity formation, in both confined and eruptive events (Kliem et al. 2014).

4.3. Eruptive Events with Hot Flux Ropes

The evidence for eruption in the AIA data is based on the appearance of post-CME loops, cusps or major opening of the AR configuration. Snapshots of eruptive events with hot flux ropes are presented in Figures 1 (panels e-f), 2, and 3. They show diverse morphologies which reflect the different orientation of the flux ropes with respect to the LOS (see Section 2).

An example of an eruptive hot flux rope event (event 115) is presented in Figure 5 (see also movie2.mp4). The event took place on 2013 November 21 in AR11895 and was associated with an M1.2-class flare. The pre-flare configuration is shown in Figure 5(a). According to the 131 Å movie, from about 10:52 loops start rising while some of the low-lying loops become brighter. After 10:55 interaction between rising loops yields an elliptical blob of emission that pushes the overlying loops and stretches the whole rising magnetic configuration. As a result, a cusp is formed underneath the rising elliptical blob (Figure 5b). We interpret the rising blob as a hot flux rope seen almost edge-on. In the next few minutes the hot flux rope grows (Figure 5c) presumably by reconnection that feeds it with new poloidal flux (e.g. Lin & van Ballegoijen 2002) and its

morphology evolves from an almost elliptical blob to a twisted/writhed structure (panels (c)-(d)). The change in morphology indicates that, in addition to its growth, the hot flux rope may exhibit rotation. The flux rope could be tracked until about 11:10 (Figure 5(e)). Its detection was not possible after that time due partly to its proximity to the edge of the AIA field of view and partly to the shorter exposure times due to the flare.

As in the case of Figure 4, we are confident that the flux rope is hot because it appears only in the 131 Å data and not in the 171/304 Å data (see the movie, and panels (f)-(i) of Figure 5). The opening of the AR’s magnetic configuration shows clearly from about 11:01 to about 11:07 in the 171 Å movie as a faint large-scale loop-like structure rises and eventually opens up.

An example of the evolution of an eruptive event with a hot flux rope seen face-on (event 25) is presented in Figure 6 (see also movie3.mp4). The event occurred on 2011 September 22 in AR11302 and was associated with an X1.4-class flare. From the beginning of the movie the preflare loops (see Figure 6a) rise and the core of the AR brightens. The first evidence of the hot flux rope appears around 10:24 as a structure consisting of thin tangled threads (Figure 6b). For clarity, we delineate its outer edge with a dotted curve (Figure 6c). Figures 6d-e follow the rise of the flux rope (see also movie3.mp4). The movie and panels (c), (f)-(i) of Figure 6 indicate that the flux rope was hot because it was visible only in the 131 Å data.

Our database contains 7 erupting hot flux rope events associated with prominence material. One example is presented in Figure 7 (see also movie4.mp4). The event occurred on 2014 February 9 and was associated with an M1.0-class flare (event 130). In the movie the upward motion of material starts at about 15:11 and shows better in 304. From about 15:18 a twisted structure appears in all three passbands which gradually grows (Figures 7a-b). At the same interval, the movie shows more prominence material ejecting in 304 Å. As time passes the 304 Å prominence forms a large twisted structure which appears much smaller in 131 and 171 passbands. In 131 Å the configuration of the twisted structure gradually evolves (Figure 7c) to form a hot flux rope. It appears first at about 15:38, then grows and eventually leaves the instrument’s field of view. In Figure 7(d)-(e) we mark the candidate flux rope structure. Its appearance resembles a flux rope seen edge-on while its spatial scale is different (i.e. smaller) than the spatial scale of the ejected material at both 171 and 131 passbands (Figure 7, panels (d)-(i)).

Overall the morphologies in event 130 imply that the prominence eruption contained primarily cool and warm material which was intermingled with very hot material that showed a flux rope configuration. The hot flux rope was located inside the upper part of the large-scale twisted structure that was formed by the cool ejected material (Figure 9i). This morphology is similar to the event presented in Zhang et al. (2012).

There are basically two patterns in the 7 events with both eruptive hot flux rope and prominence material. In four of them (two of them are the events of Figures 7 and 3a) the ejected prominence material and the eruptive hot flux rope intermingled whereas in three of them (one of them is the event of Figure 3f) the ejected prominence material was segregated from the hot flux

rope that erupts.

5. Events Without Hot Flux Ropes

There are 19 prominence eruption events without signatures of hot flux ropes in our database (PEs in Table 1). A typical example (event 33 of Table 1) is presented in Figure 8. In all PE events the erupting prominence material was detected in all three AIA passbands. At 304 Å we detect cool chromospheric plasma while at 171 and 131 passbands we detect warmer plasmas that may come either from the prominence-corona transition region (the warm plasma between the building blocks of the prominence and the adjacent hot corona, e.g. Luna et al. 2012) or from the mild heating to temperatures in excess of 2×10^5 K that erupting prominences sometimes experience (e.g. Landi et al. 2010).

LASCO observations were available for 18 of the 19 PE events (there was a LASCO data gap for event 57). An inspection of the LASCO movies showed that 17 out of the 18 PE events were associated with CMEs. This is consistent with the well-known association of prominence/filament eruptions to CMEs (i.e., Gopalswamy et al. 2003 reported that 72% of the filament eruptions they studied were associated to CMEs). We note that 5 of the 17 CMEs were flux rope CMEs.

We want to make clear that the lack of *hot* flux rope signatures for these 19 PE events does not preclude in any way the existence of a flux rope. Five of the events were associated with a flux rope CME after all. We merely argue there was no trace of *hot* flux ropes, according to our criteria in Section 2.

The database contains 24 eruptive events without the presence of a hot flux rope or a prominence (PFLs in Table 1). Figure 9 presents an example of a PFL event (event 72) associated with an M1.0-class flare on 2012 August 17 in AR11548. The top row shows the evolution of the flare in 131 Å; in panel (a) we present a pre-flare image while the image of panel (b) corresponds to one minute before the flare peak. In panel (b) a cusp-shaped morphology appears as well as bright loops underneath the cusp. These features are in agreement with the standard model of eruptive events. In panel (c), taken about 7 minutes after the flare peak, the cusp is still present although the reverse Y morphology of panel (b) is not so prominent. Just above the tip of the cusp, a faint hollow elliptical feature has been marked by an arrow. That feature could be misinterpreted as hot flux rope. However, we could not follow it with certainty in subsequent images and its appearance may not be associated with a unique physical entity; instead, its appearance may come from the alignment of the emission from the tip of the cusp with faint background emission along the line of sight. Panel (d) corresponds to the decay phase of the flare; the cusp morphology is still present, however its height has decreased. The cusp does not show in the 171 Å data (see middle row of Figure 9). It is possible that its emission was either obscured by the bright background emission or that it did not have the right temperature to show in 171 data. However, the cusp appears at 304 Å (bottom row of Figure 9) several minutes after the flare maximum (panel i) and it is probably

Si XI 303.4 Å line emission from 1.8 MK plasma (e.g., Figure 4 in Stenborg et al. 2008).

Inspection of LASCO movies shows that 20 out of the 24 PFL events were associated with CMEs, thus confirming the eruptive nature of those events.

We classified as PFLs all eruptive events that did not show clear prominence eruptions and for which we were not confident about the presence of hot flux ropes (see the discussion in Section 2 about the care we took to avoid over-interpretation of the data). But 10 out of the 20 CMEs associated with PFL events were flux rope CMEs. Therefore, some fraction (at least) of the PFL events must had flux rope configuration, but it did not conform to our identification criteria.

The database contains 53 events of confined flares with no signatures of hot flux ropes (CFLs in Table 1). The confined nature of the flares was derived from the study of the AIA data (i.e., lack of dimmings or EUV waves) and LASCO C2 observations. LASCO data were available for 50 of the events (due to a data gap, there were no LASCO observations for events 58, 59, and 60). None of them showed evidence for CMEs in agreement with the AIA data.

In Figure 10 we show a characteristic example of a CFL event (event 50) that occurred on 2012 February 6 in AR11410. We show only the 131 passband, because the evolution of the event was similar in the 171 and 304 passbands. The event was a gradual M1.0-class flare. Panel (a) shows the AR configuration at the time of the flare start, where different sets of sheared loops appear. In panel (b), at the rise phase of the flare, some of the loops appear brighter and their configuration has been simplified (at least partly). However, a new set of tangled loops has appeared southwest of the initial configuration. The image of panel (c) was taken one minute after the flare maximum while the image of panel (d) corresponds to the decay phase of the flare. Figure 1 indicates that the flare was confined because no trace of rising arcades, cusps or major opening up of the of AR’s configuration were detected.

6. Comparison with Hinode XRT data

The existence or absence of hot flux ropes in 131-Å data was checked against data obtained with the XRT on the Hinode mission. 40 events of our catalog were also observed by the XRT. These flares were observed in various combinations of thin, medium-thickness, and thick XRT filters with cadence ranging from about 30 s to about 2 minutes. The field of view was either $384'' \times 384''$ (pixel size of about $1''$) or $512'' \times 512''$ (pixel size of about $2''$) or $1536'' \times 1024''$ (pixel size of about $4''$). The thin filters have peak temperature responses from about 8 MK to about 10 MK while the medium-thickness and thick filters have peak temperature responses at about 13 MK. However, all XRT filters are able to detect a wide range of temperatures (the thin filters above 2 MK) because of their broad responses (see Narukage et al. 2011, for details on the XRT filter response functions). Therefore, checking the broadband thin-filter XRT data may be roughly equivalent to checking data from narrowband AIA channels centered at 211, 335, and 94 Å whose dominant ions are formed at 2.0, 2.5, and 6.3 MK, respectively (Lemen et al. 2012).

In Table 2 we present the statistics of the events observed by both AIA and XRT. 14 of the 40 flares (35%) contained hot flux ropes in the AIA data (4 CFRs and 10 EFRs). Therefore, the sample of events observed by both instruments represents a fairly typical subset of the whole catalog (32% of the flares of the whole AIA database contained hot flux rope morphologies; see Table 3 and Section 7). We searched for signatures of flux ropes in the XRT data using the same morphological criteria that we used for the detection of flux ropes in 131-Å AIA data.

We found that 43% (17/40) of the XRT flares showed flux rope morphologies. All of the XRT flux ropes were observed with the thin filters, while two events were also observed with the medium-thickness Al filter and one event was also observed with the thick Be and thick Al filters. 11 out of the 14 events with 131-Å hot flux ropes ($\sim 79\%$) showed flux rope morphologies in XRT data as well. A characteristic example (event 1 of Table 1) is presented in Figure 11 (panels a and b); the appearance of the flux rope is similar in both images. The three EFRs that were not detected by the XRT were rather weak events whose flux rope topology was hard to discern probably due to saturation from the flare.

Table 2 indicates that XRT detected flux rope morphologies in 6 events that showed no evidence for hot flux ropes in the AIA data (one PE, three PFLs, and 2 CFLs). In all 6 events the flux ropes were detected in thin-filter images only. A typical example appears in panels c and d of Figure 11 that show 131 Å and XRT observations, respectively, of event 53. The AIA image shows a PFL event (eruption without hot flux rope or prominence) whereas the XRT image shows a flux-rope-candidate feature that is indicated by an arrow. Its morphology bears some resemblance to the hot flux rope of event 89 (Figure 3f). The flux rope of event 53 might be too cool to show in 131 Å and too hot to show in 171 and 304 Å, but it may have the right temperature to appear in the broadband Be thin XRT image; its temperature may be higher than 2 MK and below 10 MK. Similar arguments apply to the other five events that showed flux ropes in XRT but not in AIA.

7. Conclusions

This is the first large-scale survey of EUV flare observations to assess whether hot (10 MK) flux ropes are common, irrespective of their formation time relative to the CME eruption. We considered only M- and X-class flare events as hot flux ropes are more likely to exist in association to large flares. The flux ropes were identified in 131 Å data using certain morphological criteria (Section 2). They were identified as *hot* flux ropes if they were visible only in 131 Å data and not in the 171 and 304 Å data. A summary of our results is presented in Table 3 and in the pie diagram of Figure 12. The main conclusions of our work are as follows.

- 1) 32% of the flares in our database contain clear hot flux rope morphologies (45/141). In 34 cases the flux rope erupts (EFR events) and in 11 cases it does not (CFR events). There were 70 flares associated with CMEs so a hot flux rope configuration was involved in 49% of the eruptive events.

2) The number of confined events with hot flux ropes is about three times smaller than the number of eruptive hot flux rope events whereas half of the flares of our catalog were confined. It is likely that confined hot flux ropes reach lower altitudes than eruptive ones thus hindering their identification.

3) Only a small number of hot flux ropes is seen face-on (i.e. with their axis perpendicular to the line of sight). Most of them are viewed either edge-on (i.e. with their axis parallel to the line of sight) or at intermediate angles. The smaller number of flux ropes seen face-on may result from two factors: (1) the natural tendency of AR neutral lines to lie parallel to the LOS and (2) the weaker signal due to the small LOS integration path for face-on structures compared to edge-on ones.

4) The database contains 19 prominence eruptions without signatures of hot flux rope and 7 cases of eruptive hot flux ropes accompanied with prominence material. In the latter, the hot ejected plasma appears either intermingled with the cooler ejected plasma or spatially separated from it.

5) 33 of the 34 events with eruptive hot flux ropes were associated with CMEs and 27 of them (about 80%) were clear flux rope CMEs. The remaining 6 might also be flux rope CMEs but the flux rope topology was hard to discern for several reasons: they may propagate at large angles from the plane of the sky or through areas disturbed by previous events or they may be too compact to discern their flux rope morphology (Vourlidas et al. 2013). We conclude that a hot flux rope morphology in the EUV is a very good predictor for a flux rope CME.

Based on *Yohkoh* SXT and LASCO data, Kim et al. (2005b) found higher percentages of soft X-ray ejecta associated with CMEs. However, their dataset contained a smaller percentage of confined events than ours.

6) Table 3 shows that 60% of the observed CMEs in our sample have flux rope structures while Vourlidas et al. (2013) found that at least 40% of the LASCO CMEs between 1997 and 2010 had flux rope structures. Our higher percentage could be due to a combination of reasons. First, most of our events occurred close to the limb which makes the identification of a flux rope morphology easier. Second, our database contains large events that presumably are associated with stronger than average reconnection thus facilitating the formation of hot flux ropes. Finally, lower percentage of flux rope CMEs is not surprising given the fact that the Vourlidas et al. (2013) statistics include both quiet Sun and active region eruptions that may or may not be associated with flares.

7) 40 of the events were also observed by XRT on Hinode. 35% of these flares contained hot flux ropes in AIA while 43% of them showed flux ropes in XRT data. Therefore the XRT data show that flux ropes are a rather common ingredient in events associated with M- and X-class flares. Flux ropes were detected in half of the 40 flares irrespective of the instrument used for their detection.

We found that 49% of our events have hot flux ropes but practically all CME models expect the erupting structure to be a flux rope. This raises the question of the magnetic configuration in the remaining 51% of the database (36 cases). Is there a magnetic flux rope configuration or not? We believe that there is a straightforward explanation. The flux rope exists but it is simply too cool to be detected in 131 Å and possibly too hot to show in 171 Å, 304 Å, or even, 193 Å. There is quite a substantial amount of evidence to support our assertion: (i) The higher percentage of flux rope CMEs (60%) suggests that 20% of the flux ropes, in our study, were not visible in 131 Å. (ii) the strong association between *hot* flux ropes and flux rope CMEs (80%) reflects the expected association between the length of the erupting neutral line, the amount of free magnetic energy available for the eruption and subsequently the percentage of magnetic energy available to heat the plasma. Since the maximum temperature attained during impulsive heating events is proportional to the volumetric heating (e.g., Cargill 1994; Patsourakos and Klimchuk 2006) it is anticipated that longer (shorter) flux ropes will reach lower (higher) temperatures, for a given magnetic field thus magnetic free energy. We, therefore expect a spectrum of erupting flux ropes with temperatures correlated to the available magnetic energy. As further support, we submit (i) the detection of flux ropes with the XRT in 6 events that did not show such signatures in 131-Å data (see Section 6) and (ii) the detection of a flux rope in 284 Å (~ 1.8 MK) but not in 195 Å reported by Vourlidas et al (2012) for an AR eruption during the early rise of Cycle 24. Finally, the appearance of hot flux ropes could be compromised by projection effects, loops seen along the line of sight and saturated emission. This could be especially problematic for face-on cases.

Based on the above discussion, we conclude that our estimate of 32% for the rate of occurrence of hot flux ropes in the flares above M class, and of 49% occurrence rate of hot flux ropes in the eruptive events, constitute lower limits.

An obvious extension of this work is a survey of our database to assess the timing of the formation of the eruptive hot flux ropes with respect to the initiation of the associated CMEs.

We thank the referee for his/her constructive comments. This research has been partly co-financed by the European Union (European Social Fund -ESF) and Greek national funds through the Operational Program “Education and Lifelong Learning” of the National Strategic Reference Framework (NSRF) -Research Funding Program: “Thales. Investing in knowledge society through the European Social Fund”. SP acknowledges support from an FP7 Marie Curie Grant (FP7-PEOPLE-2010-RG/268288). AV was also supported by internal JHU/APL funds.

REFERENCES

- Amari, T., Luciani, J.F., Mikić, Z., & Linker, J. 1999, ApJ, 518, L57
 Amari, T., Luciani, J.F., Mikić, Z., & Linker, J. 2000, ApJ, 529, L49
 Amari, T., Luciani, J.F., & Aly, J.J. 2004, ApJ, 615, 165

- Amari, T., Luciani, J.F., & Aly, J.J. 2005, *ApJ*, 629, 37
- Antiochos, S.K., Dahlburg, R.B., & Klimchuk, J.A. 1994, *ApJ*, 420, L41
- Antiochos, S.K., DeVore, C.R., & Klimchuk, J.A. 1999, *ApJ*, 510, 485
- Archontis, V., & Hood, A.W. 2008, *ApJ*, 674, L113
- Archontis, V., & Hood, A.W. 2012, *A&A*, 537, 62
- Archontis, V., & Török, T. 2008, *A&A*, 492, 35
- Bleybel, A., Amari, T., van Driel-Gesztelyi, L., & Leka, K.D. 2002, *A&A*, 395, 685
- Brueckner, G.E., Howard, R.A., Koomen, M.J., et al. 1995, *SoPh*, 162, 357
- Canfield, R.C., Hudson, H.S. & McKenzie, D.E. 1999, *GeoRL*, 26, 627
- Canou, A., Amari, T., Bommier, V., et al. 2009, *ApJ*, 693, L27
- Cargill, P. J. 1994, *ApJ*, 422, 381
- Chen, P. F. 2011, *Liv. Rev. Sol. Phys.*, 8, 1
- Cheng, X., Zhang, J., & Ding, M.D. 2011, *ApJ*, 732, L25
- Cheng, X., Zhang, J., Saar, S.H., & Ding, M.D. 2012, *ApJ*, 761, 62
- Cheng, X., Zhang, J., Ding, M.D., Liu, Y., & Poomvises, W. 2013, *ApJ*, 763, 43
- Cheng, X., Ding, M.D., Zhang, J., Srivastava, A.K., Guo, Y., Chen, P.F., & Sun, J.Q. 2014a, *ApJ*, 789, L35
- Cheng, X., Ding, M.D., Zhang, J., Sun, X.D., Guo, Y., Wang, Y.M., Kliem, B., & Deng, Y.Y. 2014b, *ApJ*, 789, 93
- Cheng, X., Ding, M.D., Zhang, J., Vourlidas, A., Liu, Y.D., Olmedo, O., Sun, J.Q., & Li, C. 2014c, *ApJ*, 780, 28
- Domingo, V., Fleck, B., & Poland, A.I. 1995, *SoPh*, 162, 1
- Fan, Y. 2010, *ApJ*, 719, 728
- Fan, Y., & Gibson, S.E. 2004, *ApJ*, 609, 1123
- Fan, Y., & Gibson, S.E. 2007, *ApJ*, 668, 1232
- Forbes, T.G., & Isenberg, P.A. 1991, *ApJ*, 373, 294
- Forbes, T.G., & Priest, E.R. 1995, *ApJ*, 446, 377

- Gibson, S.E., & Low, B.C. 1998, ApJ, 493, 460
- Gibson, S.E., & Fan, Y. 2006, ApJ, 637, L65
- Golub, L., DeLuca, E., Austin, G., et al. 2007, ApJ, 243, 63
- Gopalswamy, N., Shimojo, M., Lu, W., et al. 2003, ApJ, 586, 562
- Green, L.M., & Kliem, B. 2009, ApJ, 700, L83
- Green, L.M., Kliem, B., & Wallace, A.J. 2011, A&A, 526, A2
- Guo, Y., Schmieder, B., Démoulin, P., et al. 2010, ApJ, 714, 343
- Guo, Y., Ding, M.D., Schmieder, B., et al. 2012, ApJ, 746, 17
- Jacobs, C., Poedts, S., & van der Holst, B. 2006, A&A, 450, 793
- Jacobs, C., Roussev, I. L, Lugaz, N., & Poedts, S. 2009, ApJ, 695, L171
- Jiang, C., & Feng, X. 2013, ApJ, 769, 144
- Joshi, N.C., Magara, T., & Inoue, S. 2014, ApJ, 795, 4
- Karpen, J.T., Antiochos, S.K., & DeVore, C.R. 2012, ApJ, 760, 81
- Kim, Y.-H., Moon, Y.-J., Cho, K.-S., et al. 2004, JKAS, 37, 171
- Kim, Y.-H., Moon, Y.-J., Cho, K.-S., et al. 2005a, ApJ, 635, 1291
- Kim, Y.-H., Moon, Y.-J., Cho, K.-S., et al. 2005b, ApJ, 622, 1240
- Kliem, B., Forbes, T. G., Patsourakos, S., & Vourlidas, A. 2014, American Astronomical Society Meeting Abstracts #224, 224, #212.06
- Kosugi, T., Matsuzaki, K., Sakao, T., et al. 2007, SoPH, 243, 3
- Landi, E., Miralles, M.P., Raymond, J.C., et al. 2013, ApJ, 778, 29
- Landi, E., Raymond, J.C., Miralles, M.P., & Hara, H. 2010, ApJ, 711, 75
- Lee, J.-Y., Raymond, J.C., Reeves, K.K., et al. 2015, ApJ, 798, 106
- Lemen, J.R.,m Title, A.M., Akin, D.J., et al. 2012, SoPh, 275, 17
- Li, L.P., & Zhang, J. 2013, A&A, 552, L11
- Lin, J., & van Ballegooijen, A.A. 2002, ApJ, 576, 485
- Linker, J.A., & Mikić, Z. 1995, ApJ, 438, L45

- Luna, M., Karpen, J.T., & DeVore, C.R. 2012, *ApJ*, 746, 30
- Lynch, B.J., Antiochos, S.K., DeVore, C.R., Luhmann, J.G., & Zurbuchen, T.H. 2008, *ApJ*, 683, 1192
- Manchester, W. 2003, *J. Geophys. Res.*, 108, 1162
- MacNeice, P., Antiochos, S.K., Phillips, A., Spicer, D.S., DeVore, C.R., & Olson, K. 2004, *ApJ*, 614, 1028
- Narukage, N., Sakao, T., Kano, R., et al. 2011, *SoPh*, 269, 169
- Nindos, A., Patsourakos, S., & Wiegmann, T. 2012, *ApJL*, 748, L6.
- Nitta, N., & Akiyama, S. 1999, *ApJL*, 525, L57
- Ogawara, Y., Takano, T.; Kato, T., et al. 1991, *SoPh*, 136, 1.
- Ohyama, M., & Shibata, K. 1998, *ApJ*, 499, 934
- Ohyama, M., & Shibata, K. 2008, *PASJ*, 60, 85
- Patsourakos, S., & Klimchuk, J. A. 2006, *ApJ*, 647, 1452
- Patsourakos, S., Vourlidas, A., & Stenborg, G. 2013, *ApJ*, 764, 125
- Pesnell, W.D., Thompson, B.J., & Chamberlin, P.C. 2012, *SoPh*, 275, 3
- Reeves, K.K., & Golub, L. 2011, *ApJL*, 727, L52
- Roussev, I.I., Forbes, T.G., Gombosi, T.I., Sokolov, I.V., DeZeeuw, D.L., & Birn, J. 2003, *ApJ*, 588, 45
- Roussev, I.I., Sokolov, I.V., Forbes, T.G., Gombosi, T.I., Lee, M.A., & Sakai, J.I. 2004, *ApJ*, 605, 73
- Savage, S.L., McKenzie, D.E., Reeves, K.K., et al. 2010, *ApJ*, 722, 329
- Song, H.Q., Zhang, J., Chen, Y., & Cheng, X. 2014, *ApJ*, 792, L40
- Stenborg, G., Vourlidas, A. , & Howard, R. A. 2008, *ApJ*, 674, 1201
- Sun, X., Hoeksema, J.T., Liu, Y., et al. 2012, *ApJ*, 748, 77
- Titov, V.S., & Démoulin, P. 1999, *A&A*, 351, 707
- Tsuneta, S., Acton, L., Bruner, M., et al. 1991, *SoPh*, 136, 37
- van der Holst, B., Jacobs, C., & Poedts, S. 2007, *ApJ*, 671, L77

- Vourlidas, A., Syntelis, P., & Tsinganos, K. 2012, *Sol. Phys.*, 280, 509
- Vourlidas, A., Lynch, B.J., Howard, R.A., & Li, Y. 2013, *Sol. Phys.*, 284, 179
- Yan, Y., Deng, Y., Karlický, M., Fu, Q., Wang, S., & Liu, Y. 2001, *ApJ*, 551, L115
- Zhang, J., Cheng, X., & Ding, M.-D. 2012, *NatCo*, 3, 747

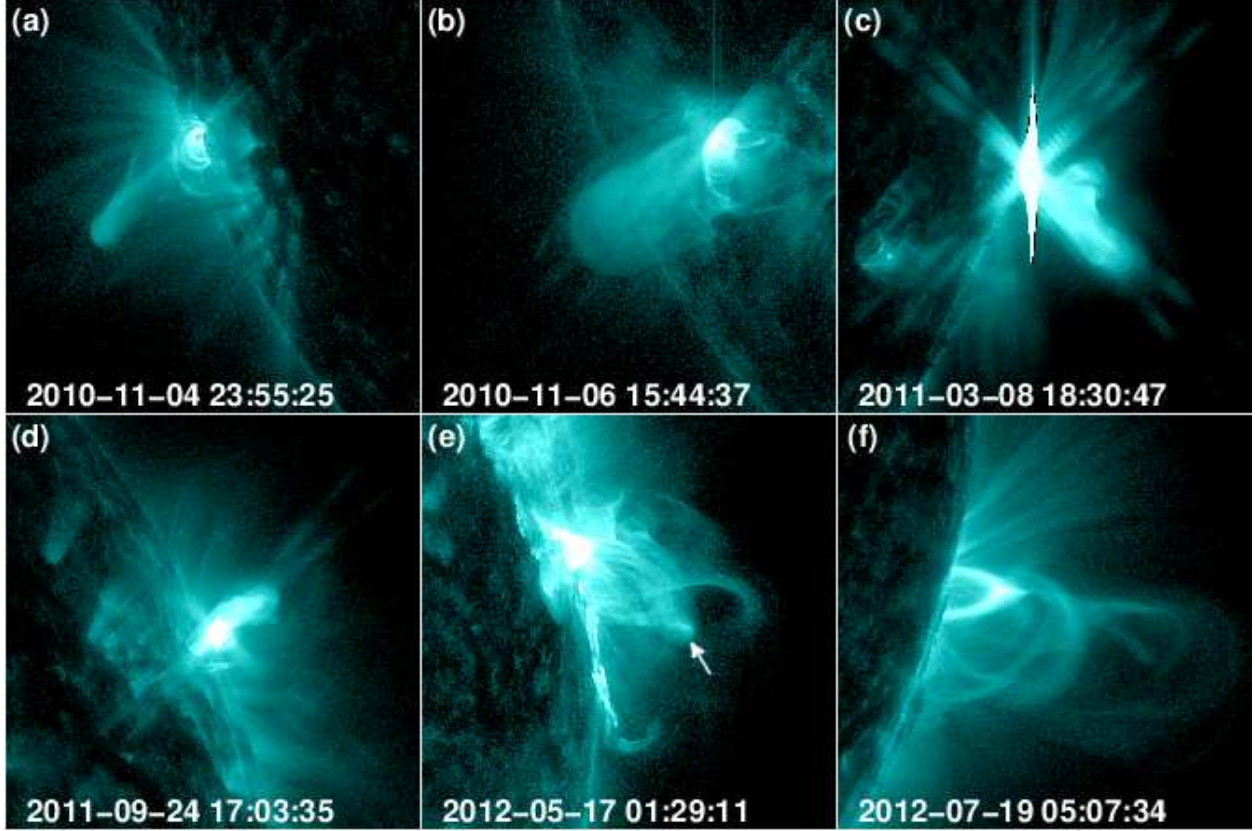


Fig. 1.— 131 Å snapshots of various events with hot flux ropes seen edge-on. Panels (a) to (f) correspond to events 1, 2, 12, 28, 61, and 69, in Table 1, respectively. The arrow marks the hot flux rope of panel (e). Date and time appears at the bottom of each image. The field of view in each image is 420×420 arcsec². In these and subsequent solar images, solar north is up, solar west to the right. (A color version of this figure is available in the online journal.)

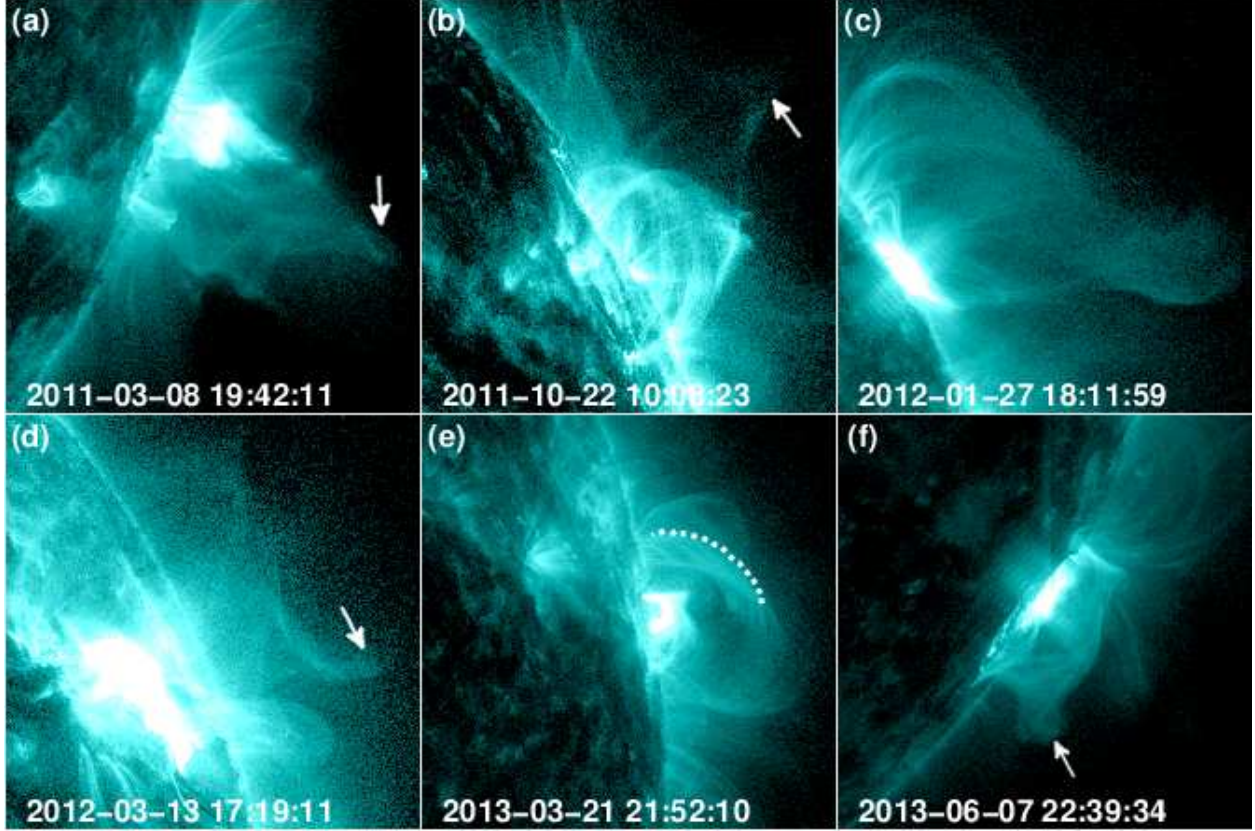


Fig. 2.— 131 Å snapshots of various events with hot flux ropes seen face-on. Panels (a) to (f) correspond to events 13, 35, 49, 54, 87, and 99, in Table 1, respectively. When appropriate arrows are used to mark the hot flux ropes. The dotted curve delineates the outer edge of the hot flux rope of panel (e). The field of view in each image is 420×420 arcsec². (A color version of this figure is available in the online journal.)

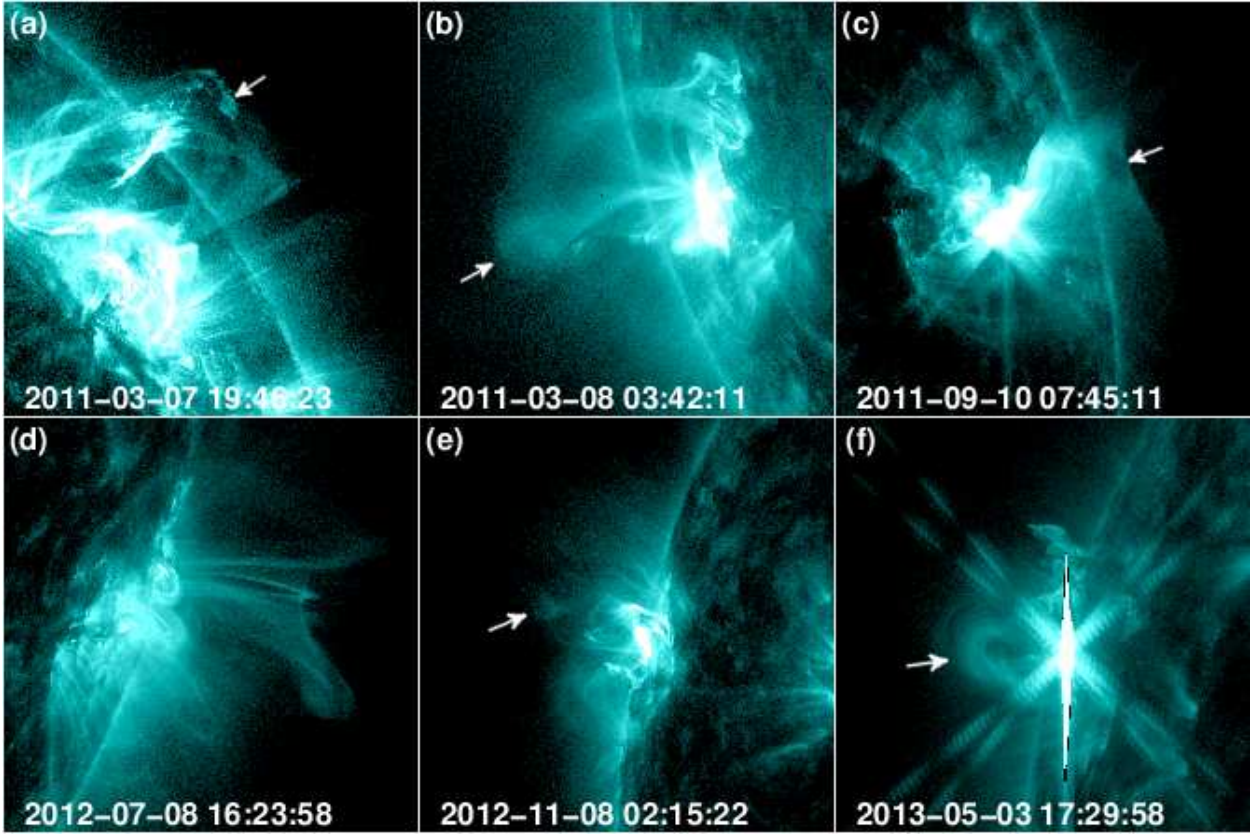


Fig. 3.— 131 Å snapshots of various events with hot flux ropes viewed from intermediate angles. Panels (a) to (f) correspond to events 8, 11, 23, 67, 81, and 89, respectively. When appropriate arrows are used to mark the hot flux ropes. The field of view in each image is 420×420 arcsec². (A color version of this figure is available in the online journal.)

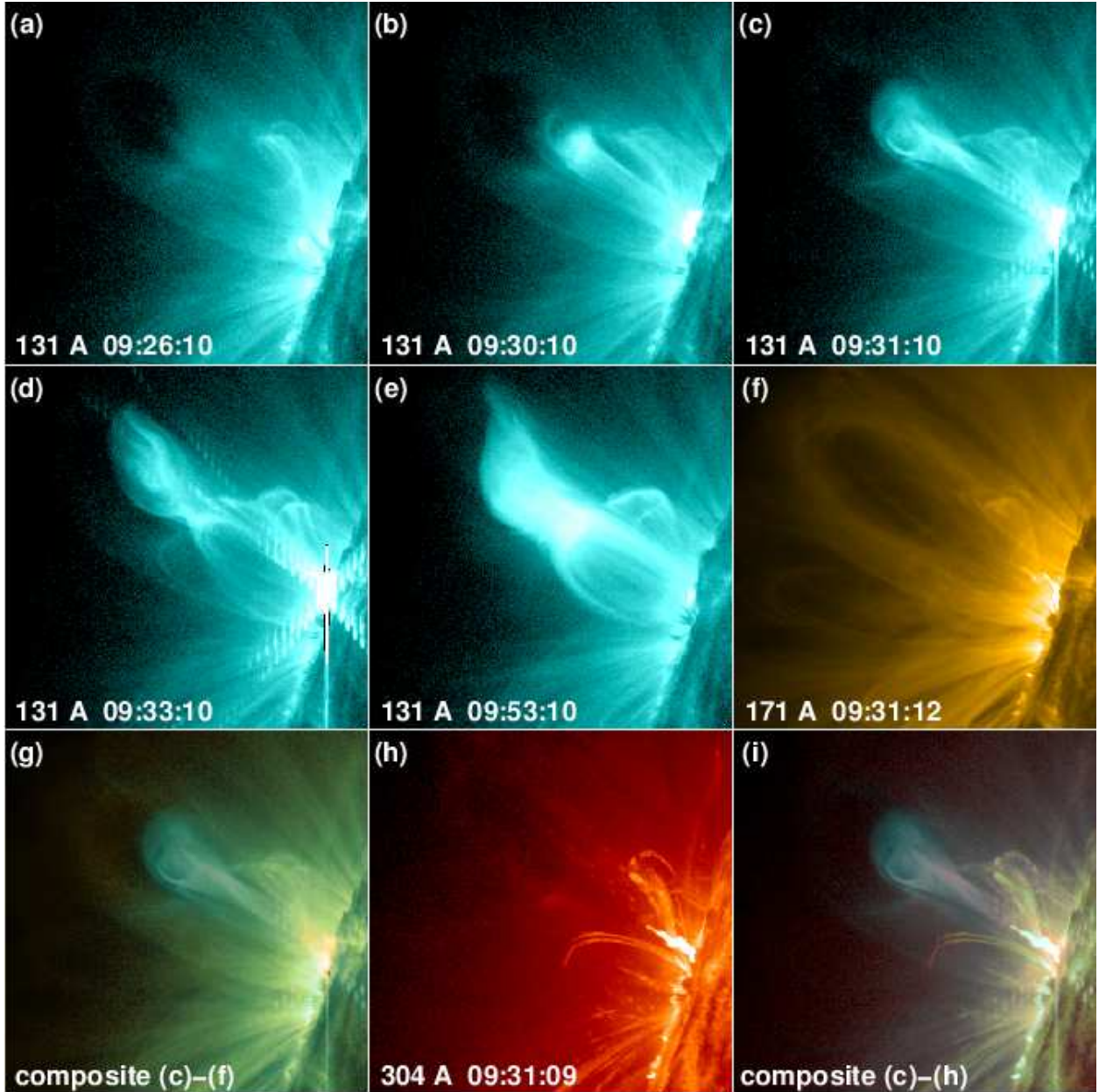


Fig. 4.— Example of a confined event with hot flux rope (CFR). The images come from event 86 that occurred on 2013 January 5. Panels (a)-(e) show 131 Å images and panels (f) and (h) show 171 and 304 Å images, respectively. Panels (g) and (i) are color composites made from the images of panels (c)-(f) and (c)-(h), respectively. The colors used in the composite images are those used for the display of the 131, 171, and 304 Å images. The field of view is 240×240 arcsec². (An animation (movie1.mp4) and color version of this figure are available in the online journal.)

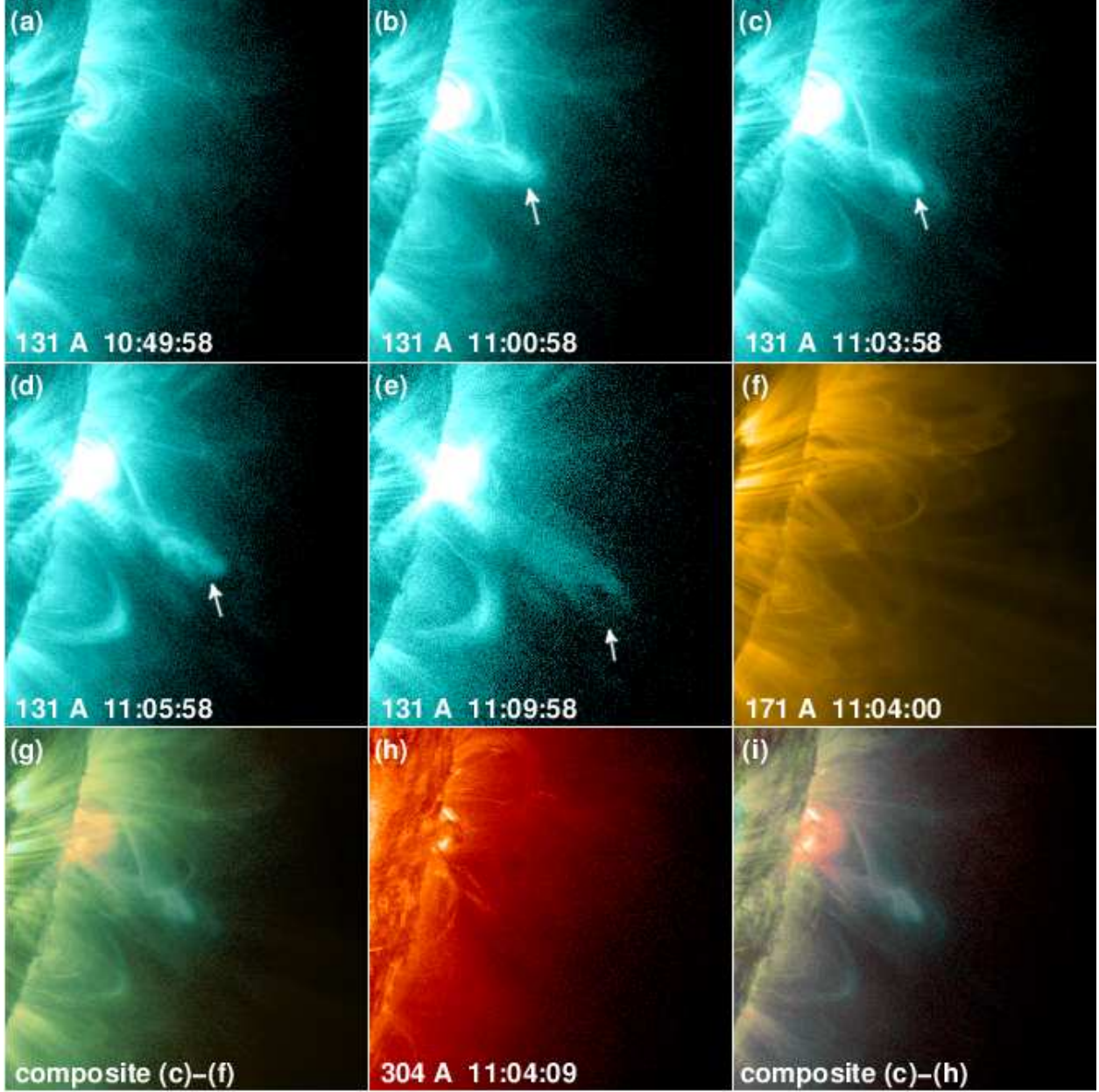


Fig. 5.— Example of an eruptive event with hot flux rope (EFR). The images come from event 115 that occurred on 2013 November 21. The format of the figure is the same as the format of Figure 4. Arrows are used to mark the hot flux rope. The field of view is 300×300 arcsec². (An animation (movie2.mp4) and color version of this figure are available in the online journal.)

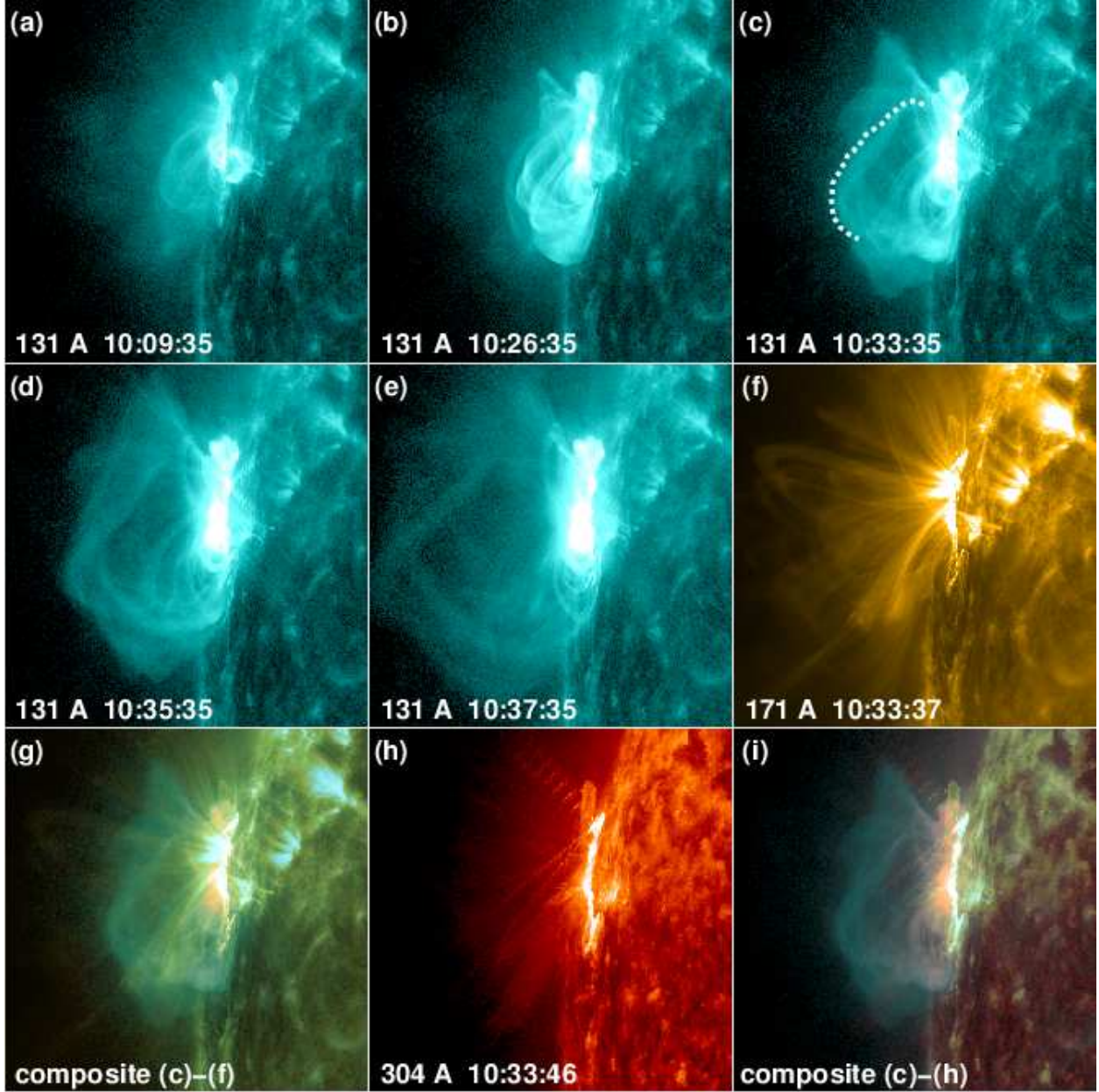


Fig. 6.— Example of an eruptive event with hot flux rope (EFR). The images come from event 25 that occurred on 2011 September 22. The format of the figure is the same as the format of Figure 4. The dotted curve of panel (c) delineates the outer edge of the hot flux rope. The field of view is 480×480 arcsec². (An animation (movie3.mp4) and color version of this figure are available in the online journal.)

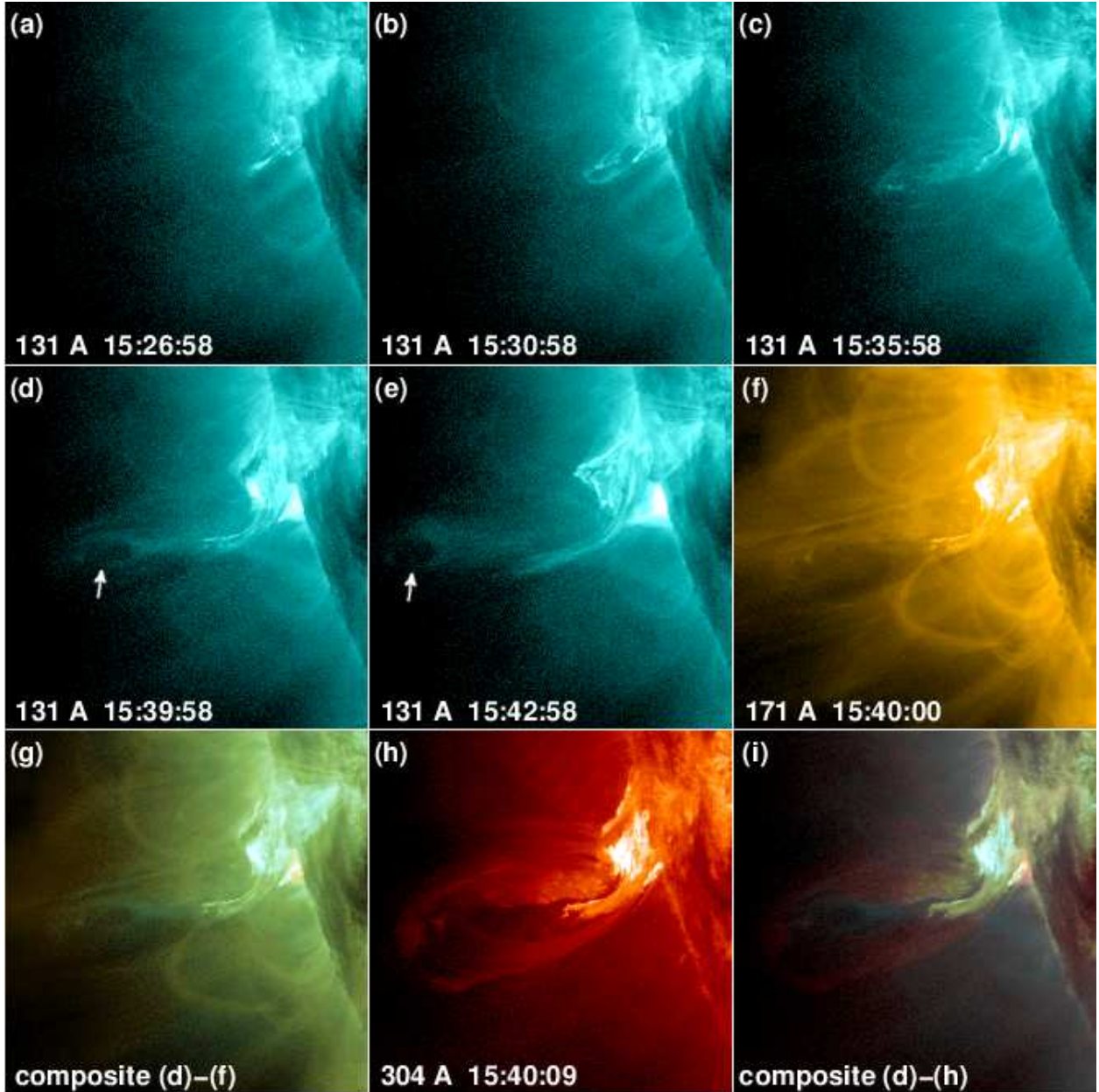


Fig. 7.— Example of an eruptive hot flux rope event (EFR) accompanied with prominence material. The images come from event 130 that occurred on 2014 February 9. The format of the figure is the same as the format of Figure 4 with the exception that the color composites of panels (g) and (i) have been made from the images of panels (d)-(f) and (d)-(h), respectively. Arrows are used to mark the hot flux rope. The field of view is 300×300 arcsec². (An animation (movie4.mp4) and color version of this figure are available in the online journal.)

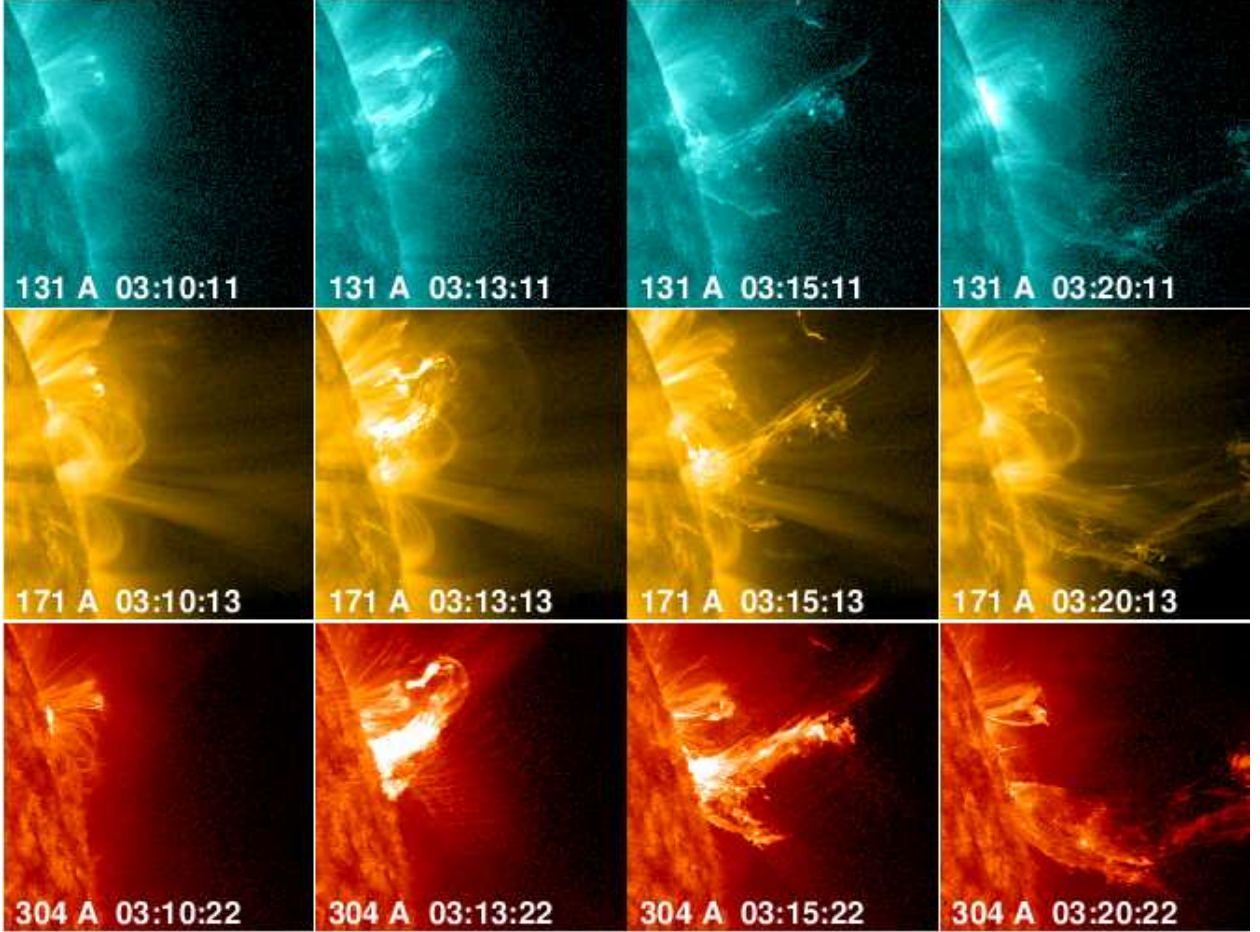


Fig. 8.— Example of a prominence eruption without hot flux rope (PE). Snapshots from the 131 (top), 171 (middle), and 304 (bottom) passband data of event 33 that occurred on 2011 October 20. The field of view is 300×300 arcsec². (A color version of this figure is available in the online journal.)

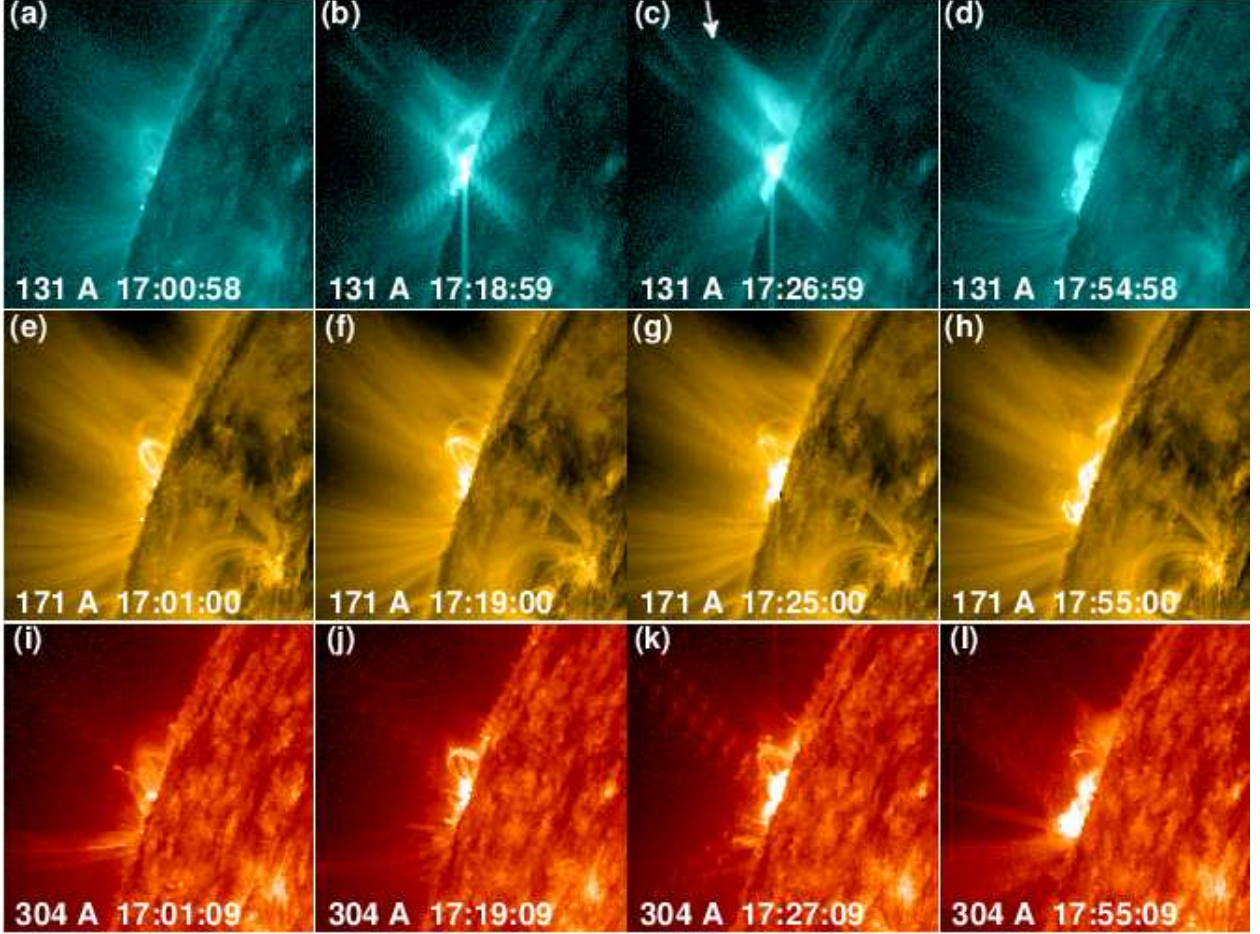


Fig. 9.— Example of an eruptive event without hot flux rope or prominence (PFL). Snapshots from the 131 (top), 171 (middle), and 304 (bottom) passband data of event 72 that occurred on 2012 August 17. The field of view is 240×240 arcsec². (A color version of this figure is available in the online journal.)

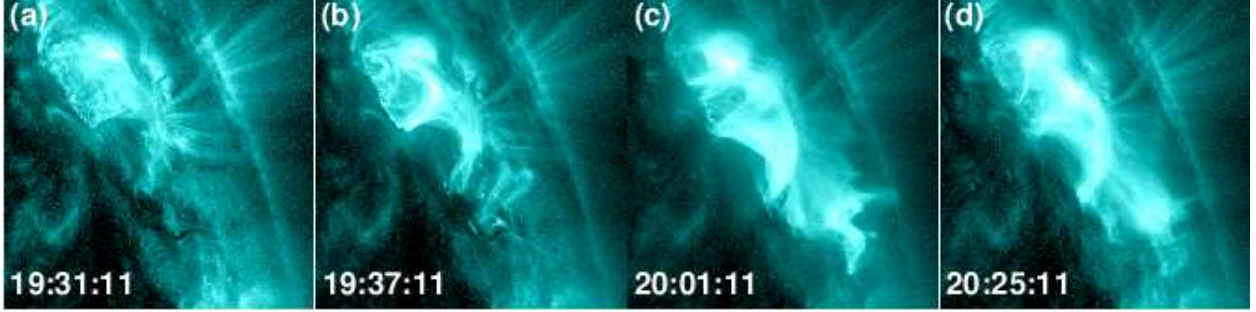


Fig. 10.— Example of a confined flare without hot flux rope (CFL). Snapshots from the 131 passband data of event 50 that occurred on 2012 February 6. The field of view is 240×240 arcsec². (A color version of this figure is available in the online journal.)

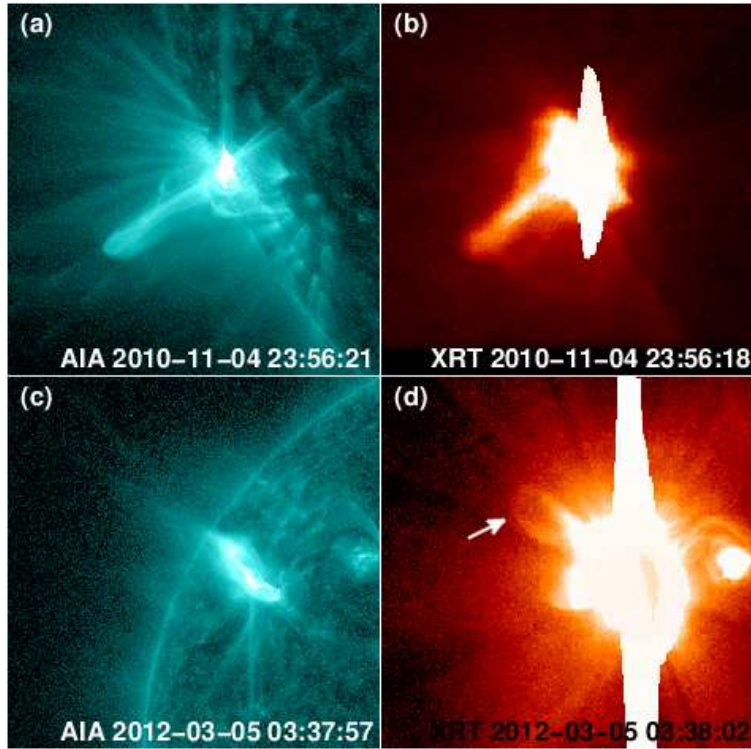


Fig. 11.— 131 Å AIA (left column) and XRT (right column) images of events 1 (panels a and b) and 53 (panels c and d). The XRT images of panels (b) and (d) have been taken with the Al mesh and Be thin filters, respectively. The field of view of panels (a) and (b) is 400×400 arcsec² and the field of view of panels (c) and (d) is 800×800 arcsec². The arrow in panel (d) is used to mark the flux rope. (A color version of this figure is available in the online journal.)

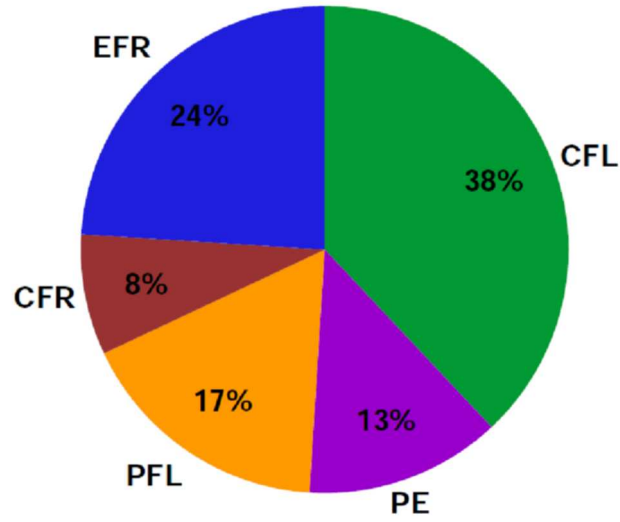


Fig. 12.— Pie diagram that shows the percentages of occurrence of the different classification groups for hot flux ropes. The acronyms are explained in Section 3. (A color version of this figure is available in the online journal.)

Table 1. Catalog of events and their classification according to AIA data

#	Date	Flare Start & Peak	Location	AR	GOES class	CME	Classification ^a
1	04 Nov 2010	23:30 23:58	S20E76	11121	M1.6	No	CFR
2	06 Nov 2010	15:27 15:36	S19E58	11121	M5.4	No	CFR
3	28 Jan 2011	00:44 01:03	N16W88	11149	M1.3	Yes (FR ^b)	PFL
4	09 Feb 2011	01:23 01:31	N16W70	11153	M1.9	No	PFL
5	24 Feb 2011	07:23 07:35	N14E87	11163	M3.5	Yes (FR)	EFR
6	07 Mar 2011	07:49 07:54	S18W75	11165	M1.6	No	PFL
7	07 Mar 2011	09:14 09:15	S17W77	11165	M1.8	No	CFL
8	07 Mar 2011	19:43 20:12	N30W50	11164	M3.7	Yes (FR)	EFR
9	07 Mar 2011	21:45 21:50	S17W82	11165	M1.5	No	CFL
10	08 Mar 2011	02:24 02:29	S17W80	11165	M1.3	No	CFL
11	08 Mar 2011	03:37 03:58	S21E72	11171	M1.5	Yes (FR)	EFR
12	08 Mar 2011	18:08 18:28	S17W88	11165	M4.4	No	CFR
13	08 Mar 2011	19:35 20:16	S19W87	11165	M1.5	Yes (FR)	EFR
14	29 May 2011	10:08 10:33	S20E64	11226	M1.4	Yes (FR)	PFL
15	07 Jun 2011	06:16 06:30	S22W53	11226	M2.5	Yes (FR)	PE
16	14 Jun 2011	21:36 21:47	N14E78	11236	M1.3	No	CFR
17	08 Aug 2011	18:00 18:10	N15W62	11263	M3.5	No	CFL
18	09 Aug 2011	03:19 03:45	N17W69	11263	M2.5	No	CFL
19	09 Aug 2011	07:48 08:05	N14W69	11263	X6.9	Yes (without FR)	PE
20	04 Sep 2011	11:21 11:45	N18W84	11274	M3.2	No	CFL
21	05 Sep 2011	04:08 04:28	N18W87	11286	M1.6	No	CFL
22	05 Sep 2011	07:27 07:58	N18W87	11286	M1.2	No	CFL
23	10 Sep 2011	07:18 07:40	N14W64	11283	M1.1	Yes (without FR)	EFR
24	21 Sep 2011	12:04 12:23	N15E88	11301	M1.8	No	CFL
25	22 Sep 2011	10:29 11:01	N09E89	11302	X1.4	Yes (FR)	EFR
26	23 Sep 2011	01:47 01:59	N24W64	11300	M1.6	No	CFL
27	24 Sep 2011	09:21 09:40	N13E61	11302	X1.9	No	CFL
28	24 Sep 2011	16:35 16:59	N23W87	11289	M1.8	No	CFR
29	24 Sep 2011	21:23 21:27	S29W67	11303	M1.2	No	CFL
30	24 Sep 2011	23:45 23:57	S28W66	11303	M1.0	Yes (without FR)	PFL
31	25 Sep 2011	02:27 02:31	N22W87	11289	M4.4	No	CFL
32	25 Sep 2011	09:25 09:35	S28W71	11303	M1.5	Yes (without FR)	PFL

Table 1—Continued

#	Date	Flare Start & Peak	Location	AR	GOES class	CME	Classification ^a
33	20 Oct 2011	03:10 03:25	N18W88	11312	M1.6	Yes (without FR)	PE
34	21 Oct 2011	12:53 13:00	N05W79	11319	M1.3	Yes (without FR)	PE
35	22 Oct 2011	09:18 11:10	N27W87	11314	M1.3	Yes (FR)	EFR
36	31 Oct 2011	14:55 15:07	N20E88	11337	M1.1	No	CFL
37	31 Oct 2011	17:21 18:07	N21E88	11337	M1.4	No	PFL
38	31 Oct 2011	18:29 18:33	N20E88	11337	M1.2	No	CFL
39	02 Nov 2011	21:52 22:01	N20E77	11339	M4.3	No	CFL
40	03 Nov 2011	10:58 11:11	N20E70	11339	M2.5	No	CFL
41	03 Nov 2011	20:16 20:27	N21E64	11339	X1.9	Yes (without FR)	PFL
42	03 Nov 2011	23:28 23:31	N20E62	11339	M2.1	No	CFL
43	15 Nov 2011	09:03 09:12	N21W72	11348	M1.2	No	CFL
44	15 Nov 2011	22:27 22:31	N18W81	11339	M1.1	No	PE
45	29 Dec 2011	13:40 13:50	S25E70	11389	M1.9	No	CFL
46	29 Dec 2011	21:43 21:51	S25E67	11389	M2.0	No	CFL
47	30 Dec 2011	03:03 03:09	S25E65	11389	M1.2	No	CFL
48	14 Jan 2012	13:14 13:18	N14E88	11401	M1.4	No	CFR
49	27 Jan 2012	17:37 18:36	N33W85	11402	X1.7	Yes (FR)	EFR
50	06 Feb 2012	19:31 20:00	N19W62	11410	M1.0	No	CFL
51	02 Mar 2012	17:29 17:46	N18E87	11429	M3.3	Yes (FR)	PFL
52	04 Mar 2012	10:29 10:52	N16E65	11429	M2.0	Yes (without FR)	EFR
53	05 Mar 2012	02:30 04:05	N19E58	11429	X1.1	Yes (FR)	PFL
54	13 Mar 2012	17:12 17:30	N17W66	11429	M7.9	Yes (FR)	EFR
55	23 Mar 2012	19:34 19:40	S23E87	11445	M1.0	No	CFR
56	16 Apr 2012	17:24 17:40	N14E88	11461	M1.7	Yes (without FR)	PE
57	05 May 2012	13:19 13:23	N11E78	11476	M1.4	No LASCO data	PE
58	05 May 2012	22:56 23:01	N11E73	11476	M1.3	No LASCO data	CFL
59	06 May 2012	01:12 01:18	N11E73	11476	M1.2	No LASCO data	CFL
60	06 May 2012	17:41 17:47	N11E63	11476	M1.3	No LASCO data	CFL
61	17 May 2012	01:25 01:47	N07W88	11476	M5.1	Yes (FR)	EFR
62	06 Jul 2012	13:26 13:30	S17E85	11519	M1.2	No	CFL
63	07 Jul 2012	08:18 08:28	S16E76	11520	M1.0	No	CFL
64	08 Jul 2012	05:41 05:46	S16W70	11515	M1.3	No	CFL

Table 1—Continued

#	Date	Flare Start & Peak	Location	AR	GOES class	CME	Classification ^a
65	08 Jul 2012	09:44 09:53	S16W70	11515	M1.1	Yes (FR)	EFR
66	08 Jul 2012	12:06 12:10	S16W72	11515	M1.4	No	CFL
67	08 Jul 2012	16:23 16:32	S14W86	11515	M6.9	Yes (without FR)	EFR
68	17 Jul 2012	12:03 17:15	S15W88	11520	M1.7	Yes (without FR)	PFL
69	19 Jul 2012	04:17 05:58	S13W88	11520	M7.7	Yes (FR)	EFR
70	27 Jul 2012	17:17 17:26	S24E71	11532	M2.7	Yes (without FR)	EFR
71	17 Aug 2012	13:12 13:19	N18E88	11548	M2.4	Yes (without FR)	PFL
72	17 Aug 2012	17:08 17:20	N19E87	11548	M1.0	Yes (without FR)	PFL
73	18 Aug 2012	03:17 03:23	N19E87	11548	M1.8	Yes (without FR)	PE
74	18 Aug 2012	16:02 16:09	N19E80	11548	M2.0	Yes (without FR)	PE
75	18 Aug 2012	22:46 22:54	N19E78	11548	M1.0	No	CFR
76	18 Aug 2012	23:15 23:22	N21E76	11548	M1.3	Yes (FR)	PE
77	30 Aug 2012	12:02 12:11	S27E85	11563	M1.3	No	CFR
78	30 Sep 2012	04:27 04:33	N12W81	11583	M1.3	No	CFL
79	09 Oct 2012	23:22 23:27	S29E86	11590	M1.7	No	CFL
80	10 Oct 2012	04:51 05:04	S29E86	11590	M1.0	No	CFL
81	08 Nov 2012	02:08 02:23	N13E89	11611	M1.7	Yes (FR)	EFR
82	11 Nov 2012	02:11 02:28	N15E89	11614	M1.0	No	CFR
83	20 Nov 2012	12:36 12:41	N11W89		M1.7	Yes (without FR)	PE
84	27 Nov 2012	15:52 15:57	N06W72	11618	M1.6	No	CFL
85	28 Nov 2012	21:20 21:28	S12W58	11620	M2.2	No	CFL
86	05 Jan 2013	09:26 09:31	N20E88	11652	M1.7	No	CFR
87	21 Mar 2013	21:42 22:04	N09W88	11692	M1.6	Yes (FR)	EFR
88	05 Apr 2013	17:34 17:48	N07E88	11719	M2.2	No	CFL
89	03 May 2013	17:24 17:32	N15E83	11739	M5.7	Yes (FR)	EFR
90	12 May 2013	20:17 20:31	N10E89	11748	M1.9	Yes (FR)	PFL
91	12 May 2013	22:37 22:44	N10E89	11748	M1.2	No	CFL
92	13 May 2013	01:53 02:16	N11E89	11748	X1.7	Yes (FR)	PFL
93	13 May 2013	11:57 12:03	N10E89	11748	M1.3	No	CFL
94	13 May 2013	15:48 16:05	N08E89	11748	X2.8	Yes (FR)	EFR
95	13 May 2013	23:59 01:11 ^c	N08E77	11748	X3.2	Yes (FR)	EFR
96	15 May 2013	01:25 01:48	N10E68	11748	X1.2	Yes (FR)	EFR

Table 1—Continued

#	Date	Flare Start & Peak	Location	AR	GOES class	CME	Classification ^a
97	20 May 2013	04:45 05:25	N09E89	11753	M1.8	Yes (FR)	EFR
98	22 May 2013	13:08 13:32	N14W87	11745	M5.0	Yes (FR)	EFR
99	07 Jun 2013	22:11 22:49	S32W89	11762	M5.9	Yes (FR)	EFR
100	21 Jun 2013	02:30 03:00	S14E73	11777	M2.9	Yes (FR)	EFR
101	03 Jul 2013	07:00 07:08	S14E82	11785	M1.5	Yes (FR)	PFL
102	09 Oct 2013	01:23 01:48	S23E71	11865	M2.8	Yes (without FR)	PE
103	25 Oct 2013	02:48 03:02	S07E76	11882	M2.9	Yes (without FR)	EFR
104	25 Oct 2013	07:53 08:01	S08E73	11882	X1.7	Yes (FR)	PFL
105	25 Oct 2013	09:43 10:11	S08E73	11882	M1.0	No	CFL
106	25 Oct 2013	14:51 15:03	S06E69	11882	X2.1	Yes (FR)	PFL
107	26 Oct 2013	19:22 19:27	S12E87	11884	M3.1	Yes (FR)	EFR
108	27 Oct 2013	12:36 12:48	S11E73	11884	M3.5	No	EFR
109	28 Oct 2013	01:41 02:03	N05W72	11875	X1.0	Yes (FR)	EFR
110	28 Oct 2013	04:32 04:41	N08W72	11875	M5.1	Yes (without FR)	PE
111	28 Oct 2013	14:00 14:05	N08W78	11875	M2.8	Yes (without FR)	PFL
112	06 Nov 2013	23:35 00:02 ^c	S11W88	11882	M1.9	Yes (FR)	PE
113	11 Nov 2013	11:01 11:18	S17E74	11897	M2.4	No	PFL
114	19 Nov 2013	10:14 10:26	S13W69	11893	X1.0	Yes (FR)	PFL
115	21 Nov 2013	10:52 11:11	S14W89	11895	M1.2	Yes (FR)	EFR
116	02 Jan 2014	02:24 02:33	S05E89	11944	M1.7	No	CFL
117	04 Jan 2014	22:09 22:52	S14W89	11936	M2.0	Yes (FR)	EFR
118	08 Jan 2014	03:39 03:47	N11W88	11947	M3.6	Yes (FR)	EFR
119	13 Jan 2014	21:48 21:51	S08W75	11944	M1.3	Yes (without FR)	PFL
120	27 Jan 2014	01:05 01:22	S16E88	11967	M1.0	No	CFL
121	27 Jan 2014	02:02 02:10	S13E88	11967	M1.1	No	CFL
122	27 Jan 2014	22:05 22:10	S14E88	11967	M4.9	No	CFL
123	28 Jan 2014	04:02 04:09	S14E88	11967	M1.5	No	CFL
124	28 Jan 2014	07:25 07:31	S10E75	11967	M3.6	Yes (without FR)	PE
125	28 Jan 2014	11:34 11:38	S10E72	11967	M1.4	Yes (without FR)	PE
126	28 Jan 2014	12:38 12:46	S15E79	11967	M1.3	No	CFL
127	28 Jan 2014	15:24 15:26	S13E88	11967	M3.5	No	CFL
128	28 Jan 2014	19:00 19:40	S14E75	11967	M4.9	No	CFL

Table 1—Continued

#	Date	Flare Start & Peak	Location	AR	GOES class	CME	Classification ^a
129	28 Jan 2014	22:04 22:16	S14E74	11967	M2.6	Yes (without FR)	PFL
130	09 Feb 2014	15:40 16:17	S16E88		M1.0	Yes (FR)	EFR
131	20 Feb 2014	07:26 07:56	S15W75	11976	M3.0	Yes (FR)	PE
132	23 Feb 2014	05:50 06:10	S16E88	11990	M1.1	Yes (without FR)	PFL
133	24 Feb 2014	11:03 11:17	S11E88	11990	M1.2	Yes (without FR)	EFR
134	25 Feb 2014	00:39 00:49	S12E77	11990	X4.9	Yes (FR)	PE
135	01 Mar 2014	13:18 13:33	S12W88	11982	M1.1	No	CFL
136	12 Mar 2014	10:55 11:05	N14W70	11996	M2.5	No	CFL
137	12 Mar 2014	22:28 22:34	N14W76	11996	M9.3	No	CFL
138	13 Mar 2014	19:03 19:19	N15W87	11996	M1.2	No	CFL
139	20 Mar 2014	03:42 03:56	S12E76	12014	M1.7	No	CFL
140	22 Mar 2014	06:58 07:02	S09W69	12011	M1.1	No	CFL
141	31 Mar 2014	07:20 08:07	S13W76	12014	M1.4	Yes (without FR)	PE

^aThe acronyms CFL, PE, PFL, CFR, and EFR are explained in Section 3.

^bFlux rope.

^cNext day.

Table 2. Events observed by both AIA and XRT

AIA Classification ^a	131 Å AIA Number of Events	XRT FRs ^b Number of Events
CFR	4	4
EFR	10	7
PE	3	1
PFL	8	3
CFL	15	2
Total	40	17

^aThe acronyms CFL, PE, PFL, CFR, and EFR are explained in Section 3.

^bFlux ropes.

Table 3. Summary of results

Classification ^a	Inner Corona	Outer Corona	
	Number of Events	Number of CMEs	Number of FR ^b CMEs
CFR	11	0	0
EFR	34	33	27
PE	19	17	5
PFL	24	20	10
CFL	53	0	0
Total	141	70	42

^aThe acronyms CFL, PE, PFL, CFR, and EFR are explained in Section 3.

^bFlux rope.